

Characterization of PN junctions of doped Mott insulators

Cite as: AIP Advances **11**, 125226 (2021); <https://doi.org/10.1063/5.0076151>

Submitted: 22 October 2021 • Accepted: 01 December 2021 • Published Online: 21 December 2021

Shu-tong Wang,  Yiou Zhang,  J. B. Marston, et al.



View Online



Export Citation



CrossMark

ARTICLES YOU MAY BE INTERESTED IN

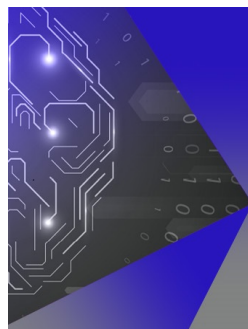
Noise characterization of ultrasensitive anomalous Hall effect sensors based on $\text{Co}_{40}\text{Fe}_{40}\text{B}_{20}$ thin films with compensated in-plane and perpendicular magnetic anisotropies

Applied Physics Letters **116**, 212404 (2020); <https://doi.org/10.1063/5.0008949>

Spin Hall effect and current induced magnetic switching in antiferromagnetic IrMn
AIP Advances **8**, 115323 (2018); <https://doi.org/10.1063/1.5059386>

PicoTesla magnetic tunneling junction sensors integrated with double staged magnetic flux concentrators

Applied Physics Letters **113**, 242401 (2018); <https://doi.org/10.1063/1.5052355>



AIP Machine Learning

Machine Learning for Applied Physics
Applied Physics for Machine Learning

**First Articles
Now Online!**

Characterization of PN junctions of doped Mott insulators

Cite as: AIP Advances 11, 125226 (2021); doi: 10.1063/5.0076151

Submitted: 22 October 2021 • Accepted: 1 December 2021 •

Published Online: 21 December 2021



View Online



Export Citation



CrossMark

Shu-tong Wang, Yiou Zhang,  J. B. Marston,  and Gang Xiao ^{a)} 

AFFILIATIONS

Department of Physics, Brown University, Providence, Rhode Island 02912, USA

^{a)} Author to whom correspondence should be addressed: Gang_Xiao@brown.edu

ABSTRACT

A heterojunction comprising a $\text{La}_{1.9}\text{Sr}_{0.1}\text{CuO}_4$ thin film on a 0.5 wt. % Nb doped SrTiO_3 single-crystal substrate was fabricated using magnetron sputtering deposition and ion milling etching techniques. Rectification has been observed in the current–voltage characteristics of the heterojunctions from 30 to 300 K. The temperature evolution of the ideality factor implies the important role of barrier inhomogeneity at the junction interface. A systematic study of capacitance as a function of frequency under different bias voltages at room temperature was also carried out. The capacitance can be explained by deep-level defects in the space charge region.

© 2021 Author(s). All article content, except where otherwise noted, is licensed under a Creative Commons Attribution (CC BY) license (<http://creativecommons.org/licenses/by/4.0/>). <https://doi.org/10.1063/5.0076151>

Heterojunctions composed of doped Mott insulators have garnered strong interest for their importance in both scientific research and potential technological applications.^{1–15} Increasing attention has been paid to heterojunctions composed of a strongly correlated perovskite oxide film and Nb doped SrTiO_3 single-crystal substrate because of the simplicity of the structure.^{3,4,8,16–19} The current (I)–voltage (V) characteristics of these heterojunctions have proved to be useful in determining superconducting gaps and Fermi level positions in electron-correlated oxides.^{5,7,8,10,17,20,21} Moreover, compared with traditional p–n or Schottky junctions where electron correlation is weak, doped Mott insulators with strong electron correlations may show different behavior in the transport properties, particularly at high frequencies. This could be useful in applications such as high-frequency rectifiers.²²

In this paper, we report the synthesis of heterojunctions comprising an epitaxial $\text{La}_{1.9}\text{Sr}_{0.1}\text{CuO}_{4-\delta}$ (LSCO) thin film grown on a 0.5 wt. % Nb doped SrTiO_3 (NSTO) substrate. The LSCO film was grown by magnetron sputtering, and the LSCO/NSTO heterojunction was patterned by physical ion-milling. In-plane electrical transport measurements have confirmed that LSCO is p-type, whereas NSTO is n-type. Superconductivity in LSCO was not observed due to a degree of oxygen deficiency. Out-of-plane I–V measurement of the LSCO/NSTO heterojunction shows good rectifying behavior, similar to a conventional p–n or Schottky junction. The temperature evolution of I–V characteristics can be

explained by barrier inhomogeneity. Comprehensive capacitance measurement over a broad range of frequency and bias voltage also reveals the important role of deep-level defects in the space charge region.

Instead of using the typical pulsed laser deposition and wet chemical etching methods to grow and process superconducting cuprates,^{10,17} we have fabricated and patterned our heterojunctions by magnetron sputtering and physical Ar ion-beam etching. We have prepared the LSCO sputtering target using the solid-state reaction of precursors in air at 1050 °C for 12 h.^{23,24} There are two different terminations on the (001) STO surface: SrO termination and TiO_2 termination. To improve quality and reproducibility of the epitaxial film growth, we followed the procedures in Refs. 25 and 26 to perform chemical and subsequently thermal treatment. A full TiO_2 termination of the NSTO substrate has been achieved. Figure 1 shows the atomic force micrograph (AFM) of the morphology of the NSTO substrate before and after chemical treatment and annealing. As can be seen, the treated NSTO substrate shows a clean terrace structure free of particulates. In addition, the step height of the terrace is ~0.4 nm, close to the lattice parameter of STO (0.39 nm). This indicates that only one termination (TiO_2) is present after the treatment.

Following the treatment of the NSTO substrates, LSCO films have been deposited through magnetron sputtering with a base pressure of 2×10^{-7} Torr. During deposition, the NSTO substrate was

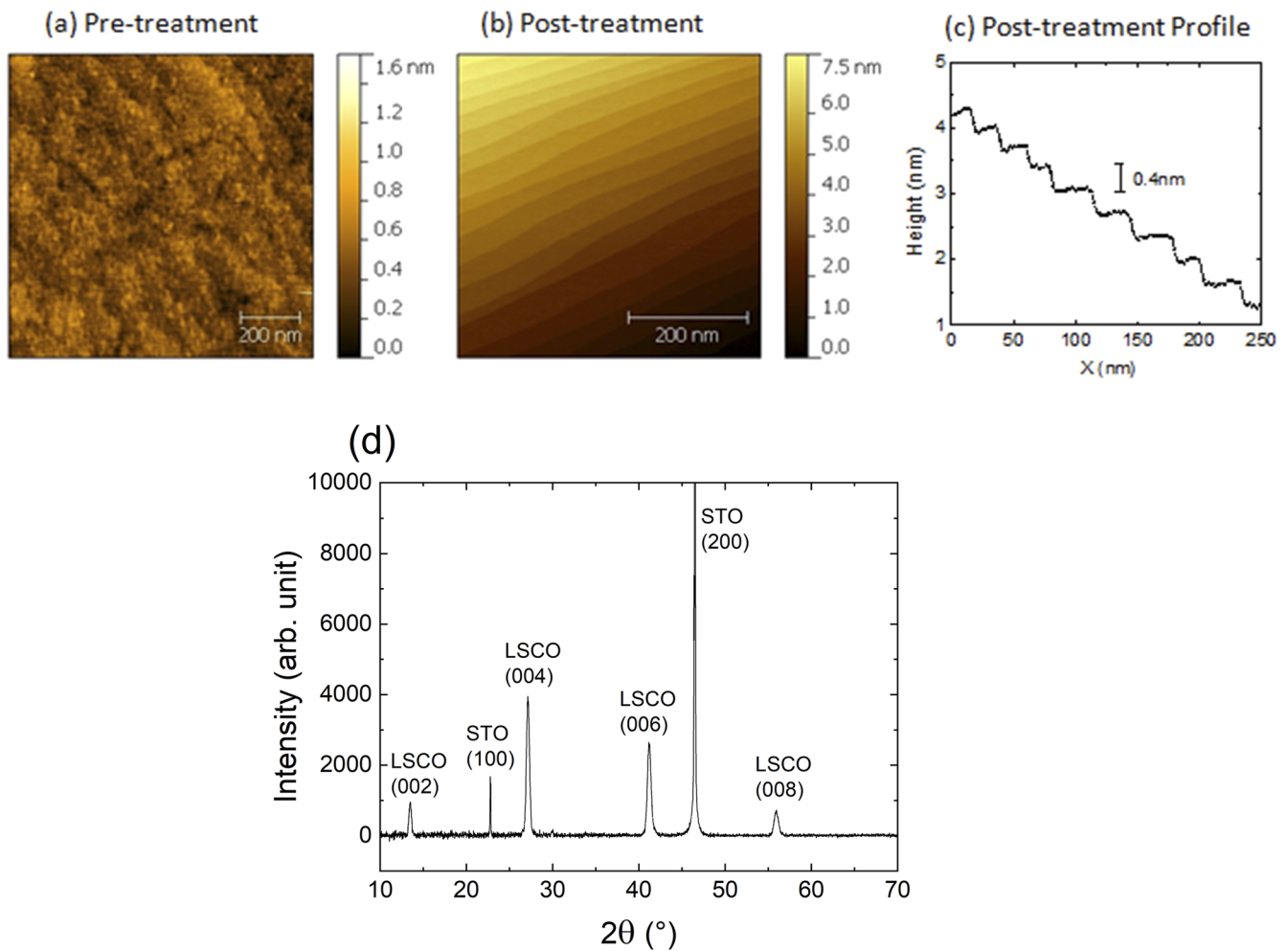


FIG. 1. Atomic force micrograph of the NSTO substrate (a) before and (b) after treatment. A cross section view of (b) is shown in (c), where atomically flat terraces with a 0.4-nm step are clearly visible. (d) XRD patterns of LSCO on NSTO substrate.

kept at a temperature of 800 °C, and the sputtering gas is 25% oxygen in argon with a total sputtering pressure of 20 mTorr.²⁷ The film's thickness is controlled by the deposition time and verified by x-ray reflectivity. The x-ray reflectivity measurement also shows small surface roughness of the deposited LSCO films. We have measured the structure of the LSCO by performing a θ - 2θ x-ray diffraction (XRD) profile using the Bruker D8 Discover x-ray diffraction system. Figure 1(d) shows the XRD pattern of a typical epitaxial LSCO film grown on the NSTO substrate. Only sharp (00n) peaks from the LSCO and the NSTO (substrate) are visible, indicating a nearly perfect c-axis orientation. All the peaks show good correspondence with previous work.^{7,10} From the full width at half maximum of the diffraction peaks, using the Scherrer equation,²⁸ the crystal domain size of LSCO is estimated to be 22 nm.

To prepare Ohmic contacts to the heterojunctions, the samples were first annealed in air at 450 °C for 30 min. After thermal

annealing, Ti(10 nm)/Au(40 nm) films were sputtered onto the top of the LSCO film and the back of the NSTO substrate to form Ohmic contacts. We used conventional photolithography and physical Ar ion-milling etching to create isolated 200 μm -diameter dot-shape heterojunctions.

First, transport properties of the LSCO film and NSTO substrate have been measured using the Quantum Design[®] Physical Property Measurement System (PPMS) from 20 to 300 K. For these in-plane transport measurements, including longitudinal resistivity and Hall coefficient measurements, the LSCO film was grown on the insulating SrTiO₃ substrate and patterned into a standard Hall bar structure. The NSTO substrate was measured using the van der Pauw configuration and Au wire-bonded contacts. Figure 2(a) shows the temperature dependence of the resistivity. From 350 to 20 K, resistivity of NSTO drops by two orders of magnitudes and remains metallic. On the other hand, LSCO is of metallic nature from 150

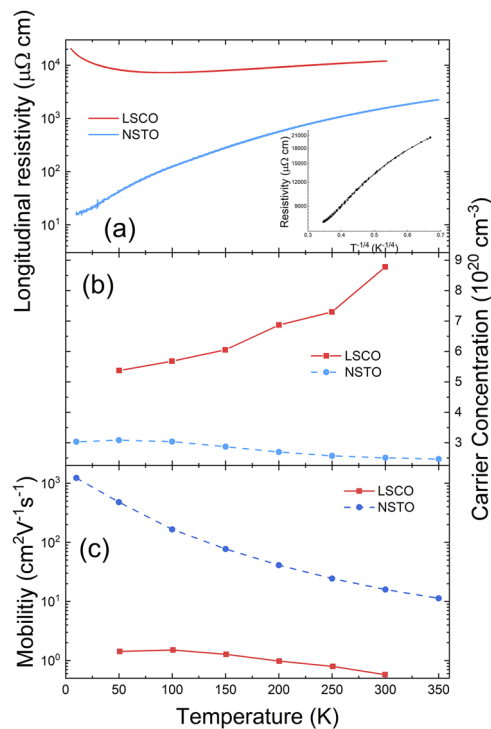


FIG. 2. (a) Longitudinal resistivity vs temperature for LSCO film and NSTO substrate. The inset shows the resistivity of the LSCO film in log scale vs $T^{-1/4}$ (only low-temperature data are included). The nearly linear relation confirms the three-dimensional VRH. (b) Carrier concentration and (c) carrier mobility in LSCO and NSTO vs temperature.

to 300 K and semiconducting like below 150 K. At low temperatures, as shown in the inset of Fig. 2(a), resistivity of LSCO fits well with $\rho(T) = \rho_0 e^{(T_0/T)^{1/4}}$, indicating that the electrical transport mechanism at low temperature is three-dimensional variable range hopping (VRH).²⁹ Superconductivity was not observed down to the lowest measurement temperature of 5 K, which is likely due to a large degree of oxygen deficiency in the sample.⁴

Hall measurements were also performed to measure the carrier type and concentration. From the sign of Hall coefficients, it is confirmed that LSCO is *p*-type and NSTO is *n*-type. Temperature dependence of Hall coefficients is shown in Fig. 2(b). As can be seen, carrier concentration in LSCO reduces by nearly half as temperature drops from 300 to 50 K. In comparison, carrier concentration in NSTO has a steady increase. It should be noted that carrier concentration in LSCO is actually higher than that in NSTO. Therefore, the rather large resistivity of LSCO mostly originates from its low carrier mobility, as shown in Fig. 2(c).

I–V characteristics of the LSCO/NSTO heterojunctions have been measured in different temperature range of 10–300 K, where a positive bias is a positive voltage applied to the top electrode in contact with the LSCO film. Figure 3(a) shows the I–V curves of one typical heterojunction. Rectification can be observed under all measurement temperatures, and the forward bias threshold increases

with decreasing temperature. The conventional thermionic emission theory for the *p*–*n* or Schottky junction, which ignores strong electronic correlations, may be used to describe the forward current according to the following equations:³⁰

$$I = I_0 \left[e^{eV/Nk_B T} - 1 \right], \quad (1)$$

$$I_0 = AA^0 T^2 e^{e\phi_B/k_B T}, \quad (2)$$

where N is the non-ideality constant, A is the sample area, A^0 is the Richardson constant ($1.202 \times 10^6 \text{ A m}^{-2} \text{ K}^{-2}$), k_B is the Boltzmann constant, and ϕ_B is the barrier height. Three sets of independent measurement have been performed over a broad temperature range. For each measurement, the barrier height ϕ_B and the non-ideality constant N are extrapolated by fitting the I–V curve using Eq. (1). As can be seen from Fig. 3(b), the barrier height ϕ_B follows a linear to quadratic relation with measurement temperature. The ideality factor significantly deviates from unity, particularly at low temperature. As shown in Fig. 2(c), the calculated ideality factor satisfies $N = 1 + T_0/T$,^{8,30} with T_0 ranging from 2300 to 7100 K. The deviation and temperature dependence of the ideality factor imply an important role of barrier inhomogeneity in the I–V characteristics of LSCO/NSTO heterojunctions. The large ideality factor and small barrier height at low temperature indicate that pure thermionic emission theory may no longer be valid, and tunneling effect must be taken into consideration.²⁰ This is particularly the case for LSCO/NSTO heterojunctions, where high carrier concentration in both LSCO and NSTO should give rise to a very narrow space charge region.

To further understand correlation between heterojunction quality and the ideality factor, we have performed I–V measurements over many LSCO/NSTO heterojunctions at room temperature. From the I–V curves, the ideality factor N and differential resistance R_0 at zero voltage were determined. For fair comparison, the resistance-area product $R_0 A$ is used. As shown in Fig. 3(d), a clear negative relationship between N and $R_0 A$ can be observed. By linear fitting, we have obtained $N = 9.48 - 0.58 \log R_0 A$. Such correlation implies that reduction in junction resistance and deviation in the ideality factor from unity may have the same physical origin. The detailed physical mechanism behind this could be related to the strong electron correlation and demands more investigation. In addition, we have observed that over-etching and intensive side-wall cleaning during the physical ion milling process would improve the heterojunction quality. This may be understood from the fact that physical ion milling unavoidably leads to side-wall redeposition. The side-wall contamination may create an undesired conducting channel. Through over-etching and side-wall cleaning processes, most of the redeposited particles may be removed.

Capacitance of LSCO/NSTO heterojunctions is critical for understanding the physical properties as well as possible applications as high-frequency rectifiers. We have measured the capacitance of LSCO/NSTO heterojunctions over a broad frequency range from 40 Hz to 5 MHz, through applying a sinusoidal voltage of 50 mV. Measurement was performed at room temperature under different DC bias voltages. A contour plot of capacitance under different bias voltages and frequencies is shown in Fig. 4(a). At low frequency and

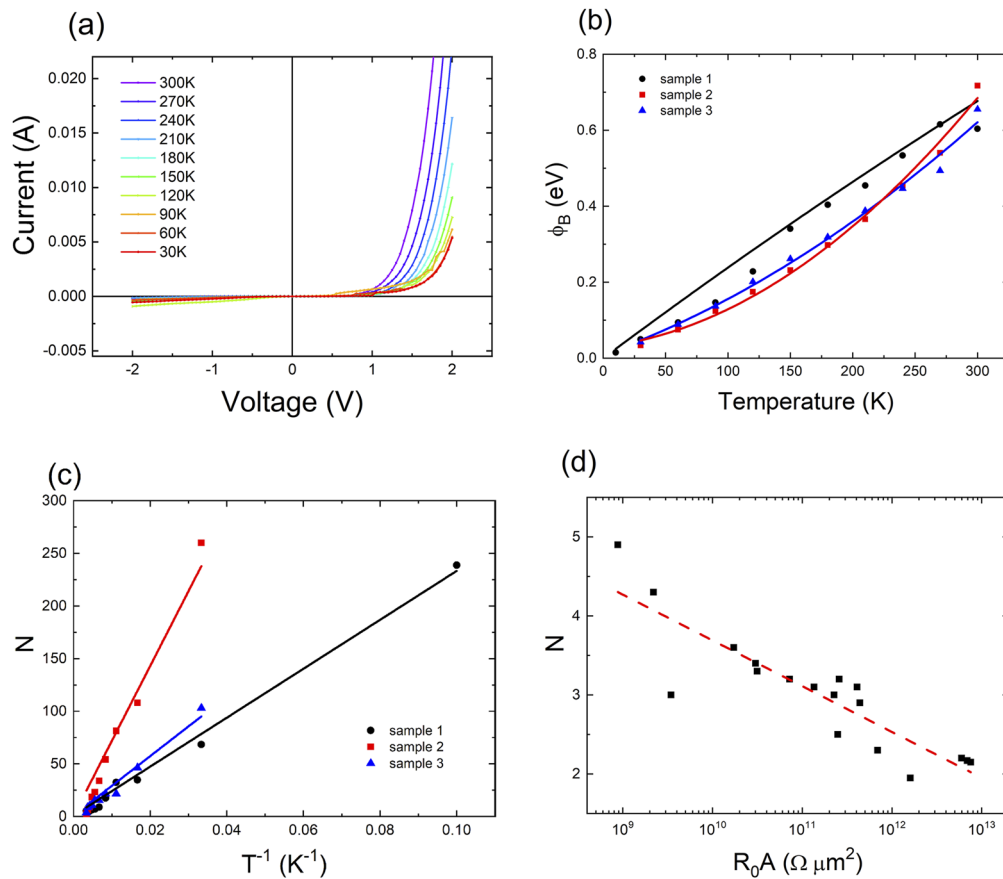


FIG. 3. (a) I–V curves of LSCO/NSTO heterojunction at different temperatures. (b) Temperature dependence of ϕ_B of three different samples. The solid lines show the quadratic fitting of the data. (c) Ideality factor N vs $1/T$, which shows a linear relation. (d) N vs R_0A in semi-log scale. The red dashed line shows the linear best fitting.

under forward bias, the heterojunction capacitance reaches peak values at ~ 0.4 V, which can be understood from the series-resistance effect.³¹ Under even larger forward bias, capacitance measurement is hindered by the large shunt conductance. From the contour plot, it is clear that capacitance of LSCO/NSTO follows different physical mechanisms at low and high frequencies. Following Zohta's work,³² we express the capacitance as

$$C(\omega) = C_{hf} + \frac{C_{lf} - C_{hf}}{1 + \omega^2 \tau_{eff}^2}. \quad (3)$$

$C_{hf} = \frac{A\epsilon\epsilon_0}{l_d}$ originates from carrier accumulation (similar to a parallel-plate capacitor), where A is the diode area and l_d is the width of the space charge region. C_{lf} comes from ionization of deep defect levels in the space charge region, and τ_{eff} is the effective relaxation time of these defects. As shown in Fig. 4(b), Eq. (3) gives a good fit for the capacitance under all bias voltages. The extrapolated C_{hf} , C_{lf} , and τ_{eff} are shown in Figs. 4(c) and 4(d). As shown in Fig. 4(c), the low-frequency capacitance C_{lf} follows $\frac{1}{C_{lf}} \propto (V_{bi} - V)$, as expected for capacitance due to defect levels in the space charge

region of p–n or Schottky diodes.^{8,9,11,16,17,20} The built-in potential V_{bi} is extrapolated as 0.91 V, close to ϕ_B from I–V curves at room temperature and values reported in previous work.^{8,17} Both C_{hf} and τ_{eff} show a steady increase as bias voltage increases. The increase in C_{hf} is likely caused by the reduced space charge region width. For applications as high-frequency rectifiers, more investigation on capacitance in the GHz and even THz range would be necessary. In addition, the heterojunction could be further optimized for minimal capacitance.

In summary, we reported on the successful synthesis of high-quality heterojunctions of epitaxial $\text{La}_{1.9}\text{Sr}_{0.1}\text{CuO}_4$ thin films on a 0.5 wt. % Nb doped SrTiO_3 single-crystal substrate using a magnetron sputtering system. In the absence of the superconductivity in LSCO films, the LSCO/NSTO heterojunctions shows a good rectification ratio. The temperature dependence of the ideality factor implies the important role of barrier inhomogeneity. At room temperature, we carried out a comprehensive capacitance measurement over a broad range of frequency and DC bias voltage. The frequency and bias voltage dependence of the junction capacitance can be well explained by a p–n junction or Schottky diode with deep-level defects in the space charge region. Our results demonstrate the feasibility of growing and

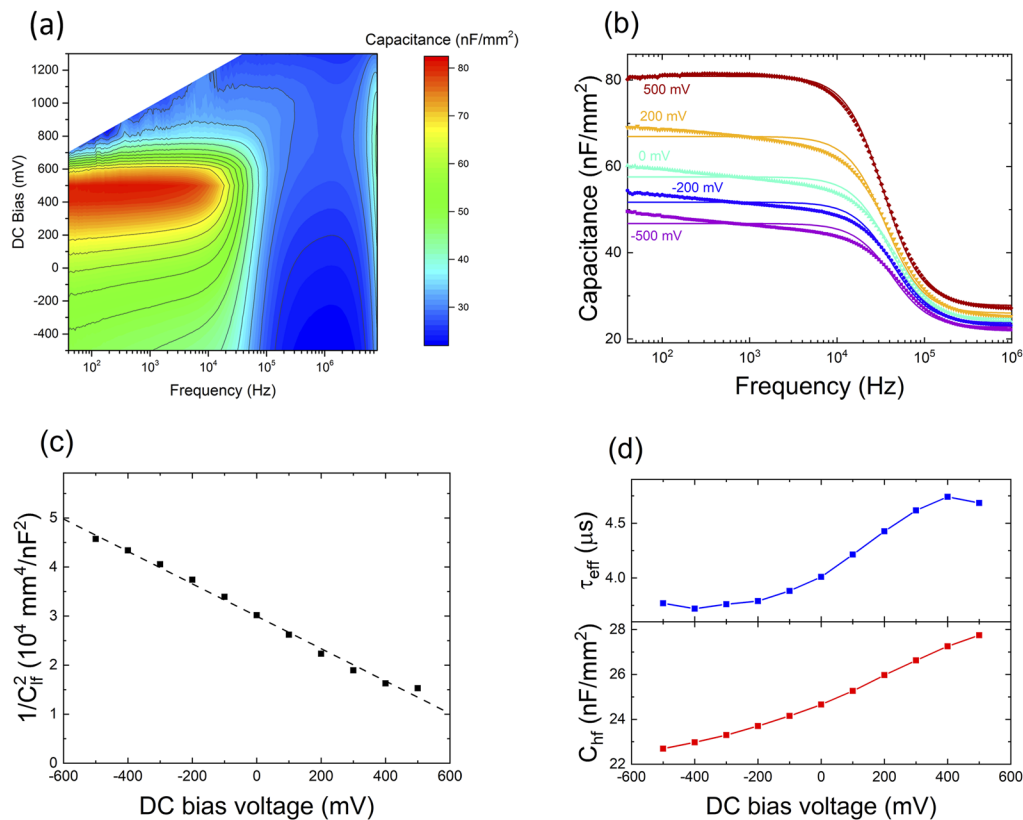


FIG. 4. (a) Capacitance contour plot vs DC bias and frequency. (b) Frequency evolution of capacitance under different bias voltages. The solid lines show best fit by Eq. (3). (c) $1/C_{hf}^2$ vs bias voltage. The dashed line shows linear best fit. The x-intercept of the fitting line gives diffusion potential, which is 0.91 V. (d) C_{hf} and τ_{eff} vs bias voltage.

patterning LSCO/NSTO heterojunctions and similar structures by magnetron sputtering and physical ion milling.

We wish to thank Vladan Mlinar, Dimenico Pacifici, and Zekun Zhuang for discussions and help. This work was supported by a Brown University Seed Award.

AUTHOR DECLARATIONS

Conflict of Interest

There are no conflicts of interest to disclose.

DATA AVAILABILITY

The data that support the findings of this study are available from the corresponding author upon reasonable request.

REFERENCES

- ¹T. Shimizu, N. Gotoh, N. Shinozaki, and H. Okushi, *Appl. Surf. Sci.* **117–118**, 400 (1997).
- ²T. Hasegawa, K. Mattenberger, J. Takeya, and B. Batlogg, *Phys. Rev. B* **69**, 245115 (2004).
- ³Z. Liu *et al.*, *Supercond. Sci. Technol.* **18**, 438 (2005).
- ⁴W. Ramadan, S. B. Ogale, S. Dhar, L. F. Fu, S. R. Shinde, D. C. Kundaliya, *et al.*, *Phys. Rev. B* **72**, 205333 (2005).
- ⁵J. R. Sun, C. M. Xiong, Y. Z. Zhang, and B. G. Shen, *Appl. Phys. Lett.* **87**, 222501 (2005).
- ⁶Y. F. Guo, L. M. Chen, M. Lei, X. Guo, P. G. Li, J. Q. Shen, and W. H. Tang, *J. Phys. D: Appl. Phys.* **40**, 4578 (2007).
- ⁷X. Q. Xiang, J. F. Qu, Y. Q. Zhang, X. L. Lu, T. F. Zhou, G. Li, and X. G. Li, *Appl. Phys. Lett.* **90**, 132513 (2007).
- ⁸J. P. Shi, Y. G. Zhao, H. J. Zhang, and X. P. Zhang, *Appl. Phys. Lett.* **92**, 132501 (2008).
- ⁹A. Podpirka and S. Ramanathan, *J. Electrochem. Soc.* **159**, H72 (2011).
- ¹⁰Y. Zhang, G. F. Wang, W. L. Li, J. Q. Shen, P. G. Li, M. Lei, and W. H. Tang, *Mod. Phys. Lett. B* **27**, 1350005 (2013).
- ¹¹F. X. Hao, C. Zhang, X. Liu, Y. W. Yin, Y. Z. Sun, and X. G. Li, *Appl. Phys. Lett.* **109**, 131104 (2016).
- ¹²J. Jia, J. Li, and G. Zhao, *J. Supercond. Novel Magn.* **31**, 1733 (2018).
- ¹³Q. Liu, J. Miao, Z. Xu, P. Liu, K. Meng, X. Xu, Y. Wu, and Y. Jiang, *Appl. Phys. Express* **12**, 051013 (2019).
- ¹⁴J. Jia, J. Gao, and G. Zhao, *J. Mater. Sci.* **54**, 1443 (2019).
- ¹⁵D. Zhang *et al.*, *Phys. Status Solidi RRL* **15**, 2000360 (2021).
- ¹⁶T. Yamamoto, S. Suzuki, H. Suzuki, K. Kawaguchi, K. Takahashi, and Y. Yoshisato, *Jpn. J. Appl. Phys., Part 2* **36**, L390 (1997).
- ¹⁷B.-S. Li, A. Sawa, and H. Okamoto, *Appl. Phys. Lett.* **102**, 111606 (2013).

- ¹⁸P. Irvin, M. Huang, F. J. Wong, T. D. Sanders, Y. Suzuki, and J. Levy, *Appl. Phys. Lett.* **102**, 103113 (2013).
- ¹⁹M. Charlebois, S. R. Hassan, R. Karan, D. Senechal, and A. M. S. Tremblay, *Phys. Rev. B* **87**, 035137 (2013).
- ²⁰A. Ruotolo, C. Lam, W. Cheng, K. Wong, and C. Leung, *Phys. Rev. B* **76**, 075122 (2007).
- ²¹Y. F. Guo, X. Guo, M. Lei, L. M. Chen, W. H. Tang, P. G. Li, X. L. Fu, and L. H. Li, *Appl. Phys. Lett.* **94**, 143506 (2009).
- ²²F. C. Sabou, N. Bodington, and J. Marston, in *2012 Lester Eastman Conference on High Performance Devices (LEC)* (IEEE, 2012), p. 1.
- ²³G. Rietveld, M. Glastra, and D. Van der Marel, *Physica C* **241**, 257 (1995).
- ²⁴K. Sreedhar and P. Ganguly, *Phys. Rev. B* **41**, 371 (1990).
- ²⁵M. Kawasaki, K. Takahashi, T. Maeda, R. Tsuchiya, M. Shinohara, O. Ishiyama, T. Yonezawa, M. Yoshimoto, and H. Koinuma, *Science* **266**, 1540 (1994).
- ²⁶G. Koster, B. L. Kropman, G. J. H. M. Rijnders, D. H. A. Blank, and H. Rogalla, *Appl. Phys. Lett.* **73**, 2920 (1998).
- ²⁷N. Terada, H. Ihara, M. Hirabayashi, K. Senzaki, Y. Kimura, K. Murata, and M. Tokumoto, *Jpn. J. Appl. Phys., Part 2* **26**, L508 (1987).
- ²⁸A. L. Patterson, *Phys. Rev.* **56**, 978 (1939).
- ²⁹C. Yang, B. Liu, G. Liu, F. Diao, H. Yang, and Y. Wang, *Solid State Ionics* **319**, 28 (2018).
- ³⁰J. H. Werner and H. H. Güttler, *J. Appl. Phys.* **69**, 1522 (1991).
- ³¹P. Chattopadhyay and B. Raychaudhuri, *Solid-State Electron.* **36**, 605 (1993).
- ³²Y. Zohta, *Solid-State Electron.* **16**, 1029 (1973).